Scripta Materialia 185 (2020) 51–55

Contents lists available at ScienceDirect

Scripta Materialia

journal homepage: www.elsevier.com/locate/scriptamat

Co-segregation of Mg and Zn atoms at the planar η_1-precipitate/Al matrix interface in an aged Al–Zn–Mg alloy

Bingqing Cheng[a,1], Xiaojun Zhao[b,1], Yong Zhang[a,1], Houwen Chen[b,*], Ian Polmear[a], Jian-Feng Nie[a,*]

[a] Departsment of Materials Science and Engineering, Monash University, Victoria. 3800, Australia
[b] College of Materials Science and Engineering, Chongqing University, Chongqing 400044, PR China

ARTICLE INFO

Article history:
Received 28 January 2020
Revised 27 March 2020
Accepted 3 April 2020

Keywords:
Aluminium alloys
Interface segregation
Energy-Dispersive X-ray Spectroscopy
High-angle annular dark field
Deep neural network based calculation and simulation

ABSTRACT

Using aberration-corrected scanning transmission electron microscopy, the interface between η_1-precipitates and Al matrix in the aged Al–2.12Zn–1.71Mg (at.%) alloy has been investigated. Atomic-resolution X-ray dispersive spectroscopy mapping reveals the occurrence of co-segregation of Mg and Zn atoms in the $\{002\}_\alpha$ habit plane of the $\eta_1(MgZn_2)$ precipitates. Site-specific Mg atoms segregate outside the concave of an outermost zig-zag Zn-rich layer of the η_1 habit plane. Zn segregation surround the segregated Mg atomic columns was also observed. Hybrid molecular dynamics (MD) and Monte Carlo (MC) atomistic simulations with the accuracy of density functional theory indicate the site-specific segregation is energetically favourable.

Alloys based on the Al–Zn–Mg systems may develop high strength upon aging due to precipitation hardening. The precipitation sequence of this ternary system has been reported as follows: Super-saturated solid solution (SSSS) → GP zones (GP I and GP II) → η' phase → η phase ($MgZn_2$). The η phase is known as C14 Laves phase with the space group of $P6_3/mmc$ [1]. 12 types (η_1-η_{12}) of η phase with different orientation relationships and morphologies have been reported [2–4], including rods (η_5-η_7) or plates (η_2-η_4) on $\{111\}_\alpha$ habit plane and rods (η_9) or plates (η_1) on $\{001\}_\alpha$ habit plane. The formation of η-type precipitates on $\{111\}_\alpha$ habit plane from metastable η' precipitates has been reported [5]. However, the nucleation conditions or growth mechanisms of η-type precipitates on $\{001\}_\alpha$ habit plane have not been fully studied. Recently, Bendo et al. [6] have reported a HAADF-STEM image of η_1 phase obtained along the $[1\bar{2}10]_{\eta_1}$ direction that reveals an interesting zig-zag stacking structure at the η_1/Al interface parallel with $\{111\}_\alpha$ habit plane. However, the chemical composition and the structure of this interface are not clear. Moreover, identifying Mg columns in the Al matrix using the Z-contrast high-angle annular dark-field scanning transmission electron microscopy (HAADF-STEM) technique is challenging because the Z-contrast is roughly proportional to the square of Z (atomic numbers of atoms). However, if atomic-resolution energy-dispersive X-ray spectrometry (EDXS) mapping technique is used, in combination with atomic-resolution HAADF-STEM imaging, to obtain the information along $[0001]_{\eta_1}$ and $[1\bar{2}10]_{\eta_1}$ directions, site-specific segregation of Mg and Zn atoms in this interface could be revealed and established. Such findings may be useful to the understanding of the growth mechanism of η-type precipitates with the $\{001\}_\alpha$ habit plane.

Cast ingots with a nominal composition of Al-2.12 at.%Zn-1.71at.%Mg (or Al-5 wt.%Zn-1.5 wt.%Mg) were prepared. Small samples cut from the ingots were homogenized at 460 °C for 24 h, followed by water quenching to room temperature and cold-rolling to sheets of 0.5 mm thickness. The sheets were solution treated at 460 °C for 1 h and then artificially aged at 150 °C for 50 h. Thin foils for HAADF-STEM and EDXS observations were prepared by mechanical grinding and ion-beam milling. The sample was milled using Gatan PIPS 695 at −70 °C. The ion beam energy and angle were initially 5 keV and 6°, but reduced to 2 keV and 2°, once a small hole forms, to trim the sample for 30 min. HAADF-STEM and EDXS were performed in a Cs-corrected FEI Titan G^2 60–300 ChemiSTEM operated at 300 kV and 120 kV, respectively. 300 kV was used for the acquisition of HAADF-STEM images, and 120 kV for EDXS-STEM maps. The HAADF-STEM images were Fourier filtered with a circular aperture encompassing all visible spots in the Fourier transform pattern in Digital Micrograph software. Besides, they were appropriately adjusted for brightness and contrast in the

* Corresponding authors.
E-mail addresses: hwchen@cqu.edu.cn (H. Chen), jianfeng.nie@monash.edu (J.-F. Nie).
[1] Contributed equally.

https://doi.org/10.1016/j.scriptamat.2020.04.004
1359-6462/

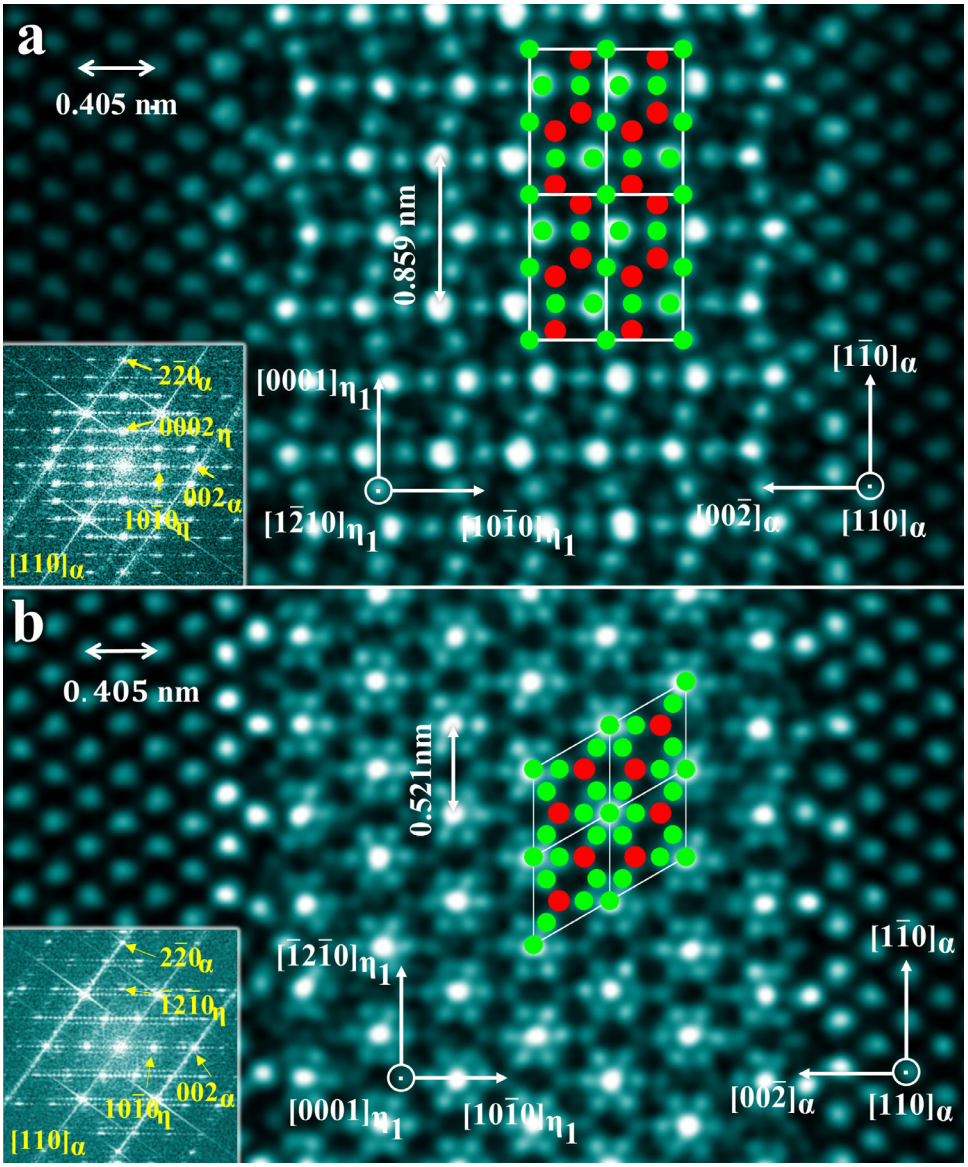

Fig. 1. (a, b) Atomic-resolution HAADF-STEM images of a η_1 precipitate plate viewed along $[110]_\alpha$. The inserts at the bottom left corner in (a) and (b) are FFT patterns of image (a) and (b) respectively. Red and green circles represent Mg and Zn atoms respectively. (For interpretation of the references to colour in this figure legend, the reader is referred to the web version of this article.)

same software. For atomic-resolution EDXS maps, they were just appropriately adjusted for brightness, contrast and gamma value in Esprit software, without any other adjustments. HAADF-STEM image simulation was performed with μSTEM software package [7]. The sample thickness used for STEM image simulation is 30 nm, which was obtained experimentally from the foil using position average convergent beam electron diffraction (PACBED) patterns. The large misfit (~9.09%) along $\langle 1\bar{2}10\rangle_{\eta_1}//\langle 110\rangle_\alpha$ makes it impossible to build small supercells (<500 atoms) for routine density functional theory (DFT) calculations. Instead, a deep potential molecular dynamics method was adopted which can achieve the accuracy of Quantum Mechanics in such simulations [8,9]. A potential was built by training a deep neural network model with 362,992 DFT calculated configurations (32–236 atoms per configuration, labelled with energies and forces) [8,9]. These configurations include binary and ternary intermetallic, single elemental structures (face-centred cubic (FCC), body-centred cubic (BCC) and hexagonal close pack (HCP)) and solute segregation around defects (stacking faults, dislocations and grain boundaries) in FCC Al. DFT calculations were carried out using Vienna ab initio Simulation Package (VASP) with generalised-gradient-approximation (GGA) method and Perdew-Burke-Enzerhof (PBE) parameterization [10–13]. After-training validation suggested that the root-mean-square errors of the trained deep neural network potential were 4 meV/atom (energy) and 800 meV/nm relative to DFT calculated data sets. Such accuracies were good enough for deep neural network based potentials and should give predication comparable to typical DFT calculations (uncertainty ~ 5 meV/atom) [14,15]. Using this method, the energy of a supercell with 2364 atoms was calculated. Such large supercell guarantees the mismatch between 20 layers of $(110)_\alpha$ plane and 11 layers of $(11\bar{2}0)_\eta$ plane to ~ 0. Supercells with different interfacial structures (different solute segregation patterns) were relaxed using the conjugate gradient method (energy tolerance: 10^{-10}, force tolerance: 10^{-8}). Hybrid molecular dynamics (MD), 2 fs per step, and Monte Carlo (MC), 1 step per 100 MD steps, atomistic simulations were performed using the large-scale atomic/molecular massively parallel simulator (LAMMPS) software package [16]. The simulation is expected to reach a thermodynamic equilibrium state when no MC swaps are successful in 10,000 consecutive MC steps.

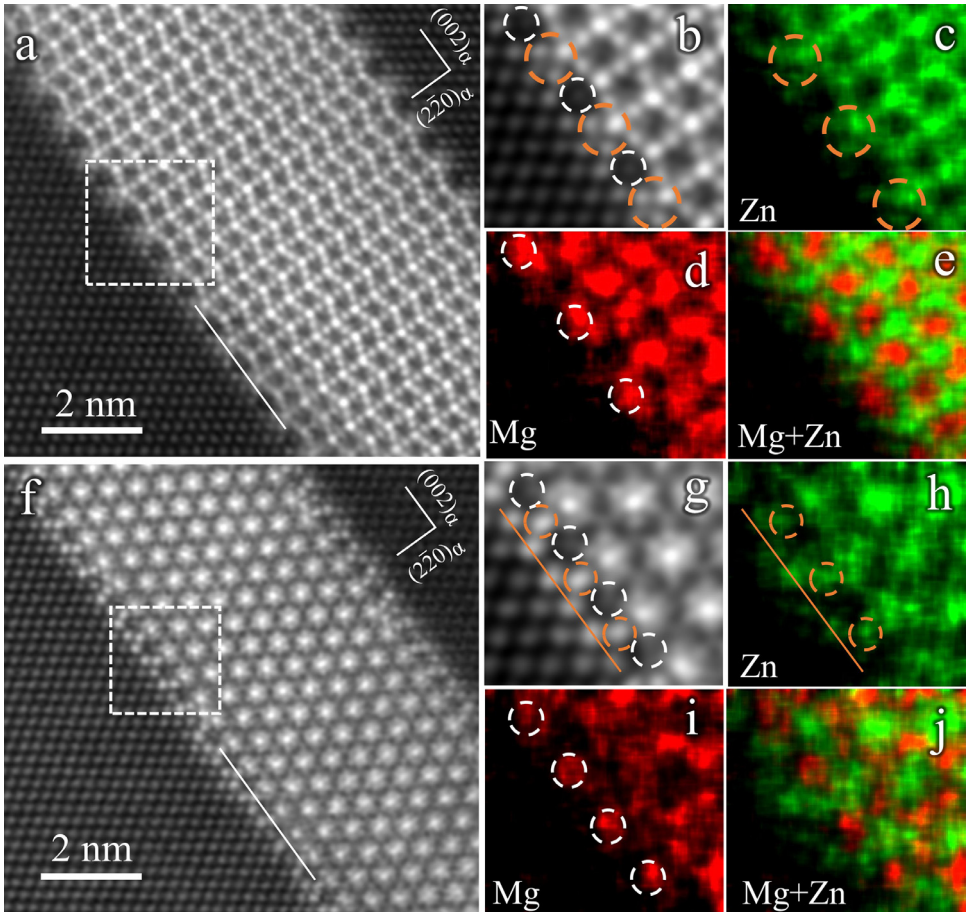

Fig. 2. (a, b, f, g) HAADF-STEM images of η_1/Al habit plane interface (c–e) EDXS mapping of the area in (b). (h-j) EDXS mapping of the area in (g). (c, h) Zn map, (d, i) Mg map, (e, j) Zn and Mg map.

Fig. 1a shows an atomic-resolution HAADF-STEM image of a plate-like precipitate viewed along $[110]_\alpha$. The distribution of atomic columns within the precipitate is consistent with that of the η_1 reported in previous studies [2,6]. The habit plane of this precipitate is parallel to $\{002\}_\alpha$, and its orientation relationship is such that $(10\bar{1}0)_{\eta_1}//(002)_\alpha$; $[1\bar{2}10]_{\eta_1}//[110]_\alpha$, as indicated by the FFT pattern in Fig. 1a. For this orientation relationship, $[0001]_{\eta_1}$ is parallel to $[1\bar{1}0]_\alpha$. Therefore, it is also possible to detect η_1 precipitates with their $[0001]_{\eta_1}$ parallel to the $\langle 110\rangle_\alpha$ beam direction. Examination of precipitates indicated that such an orientation indeed exists, and an example is provided in Fig. 1b. Inspection of the arrangement of atoms in the image further confirms the structure and orientation relationship being consistent with those of η_1. Assuming that the lattice parameter of α-Al is $a_\alpha = 0.405$nm, lattice parameters of η phase were measured to be $a_{\eta_1} = 0.521$nm and $c_{\eta_1} = 0.859$nm. The measured lattice parameters are close to those ($a = 0.5221(3)$ nm, $c = 0.8567(6)$ nm) reported by Komura [1]. The misfit along $[1\bar{2}10]_{\eta_1}//[110]_\alpha$ is calculated to be $[d_{(110)_\alpha} - d_{(1\bar{2}10)_{\eta_1}}]/d_{(110)_\alpha} = 9.09\%$. The experimental observations made in the present study, Fig. 1a and b, confirm the structure model proposed by Komura [1].

Figs. 2a and b show HAADF-STEM images of the η_1/Al habit plane interface along $[1\bar{2}10]_{\eta_1}//\ [110]_\alpha$, similar to that shown in Fig. 1a. A zig-zag layer comprising Zn-rich columns separates the η_1 phase from the adjacent Al matrix phase. The layer immediate outside this zig-zag layer (labelled by solid white line in Fig. 2a) shows different brightness from both η_1 and matrix phases, indicating the possible presence of solute segregation at this interface. In this layer, columns out of the concave (marked by white circles in Fig. 2b) of the zig-zag layer show lower brightness, and the two columns (marked by orange circles in Fig. 2b) between two adjacent white circles have higher brightness, than that of columns in the Al matrix. Because the brightness of an atomic column in a HAADF-STEM image is approximately proportional to the square of Z, the brighter columns indicate an enrichment in Zn ($Z_{Zn} = 30$), while the darker columns indicate a possible enrichment in Mg ($Z_{Mg} = 12$) compared with those in the Al matrix ($Z_{Al} = 13$). Since it is difficult to distinguish Mg and Al in HAADF-STEM images, atomic-resolution EDXS mapping was used to examine the identity of the segregated solutes. Fig. 2c and e show Zn, Mg and (Zn+Mg) EDXS maps of the interface layer. These maps clearly reveal that Mg atoms segregate to the sites marked by white circles and that Zn atoms segregate to the sites marked by orange circles. EDXS mapping along an orthogonal orientation of the precipitate, i.e. $[0001]_{\eta_1}$, Fig. 2g–j, confirms such site-specific segregation in this layer. Moreover, columns labelled by the solid orange line in Fig. 2g, seem to be rich in Zn atoms, Fig. 2h.

The phenomenon of solute segregation at interfaces between precipitates and their surrounding matrix has been observed in some aluminium and magnesium alloys [17–27]. Mg and Ag atoms segregate to the Ω/Al interface in aged Al–Cu–Mg–Ag alloys, which reduced the misfit strain and stabilizes the Ω/Al interface structure [17]. Ag atoms segregate to θ'/Al interface in aged Al–Cu–Ag alloys, lowering the chemical component of the interfacial energy [21]. Ag atoms segregate to interphase boundaries of $Mg_{17}Al_{12}$ in aged Mg–7Al–2Sn–0.7Ag (wt.%) alloys, and this is correlated with re-

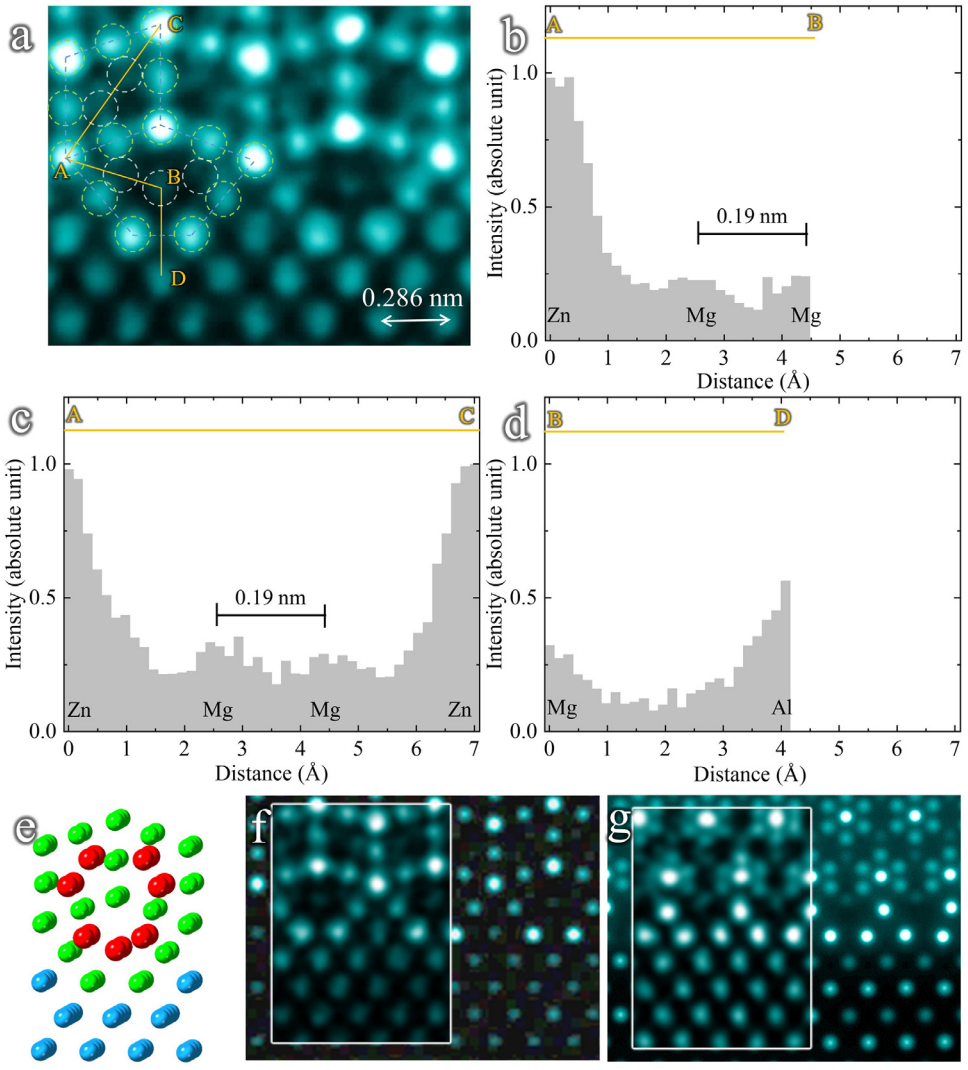

Fig. 3. (a) Enlarged HAADF-STEM image of the η_1/Al habit plane interface viewed along $[1210]_{\eta_1}//[110]_{\alpha}$. Green and white circles indicate Zn and Mg atomic columns, respectively. (b) The intensity profile of the solid orange line from the centre of atomic column A to the centre of atomic column B in image (a). (c) The intensity profile of the solid orange line from the centre of atomic column A to the centre of atomic column C in image (a). (d) The intensity profile of the solid orange line from the centre of atomic column B to the centre of atomic column D in image (a). (e) 3D schematic model of the atomic structure of the η_1/Al interface. Blue, green and red spheres represent Al, Zn and Mg, respectively. (f-g) Simulated $[1210]_{\eta_1}$ and $[0001]_{\eta_1}$ HAADF-STEM images, respectively. Insets in (f) and (g) are experimental images. (For interpretation of the references to colour in this figure legend, the reader is referred to the web version of this article.)

fined precipitates and increased number density of the precipitates [26].

To establish the precise distribution of solute atoms in the η_1/Al interface, an enlarged HAADF-STEM image (Fig. 3a) of the interface, viewed along $[1\bar{2}10]_{\eta_1}//[001]_{\alpha}$, was carefully analysed. There are three distinguishable atomic columns observed outside the concave of the zig-zag Zn-rich layer, as labelled by white circles in Fig. 3a. To accurately establish the positions of these columns, the intensity profile between two nearby columns at the interface is shown in Fig. 3b. Furthermore, the intensity profile of Mg-rich columns inside the η_1 phase is shown in Fig. 3c. Two distinguishable low-intensity peaks having similar intensity are observed in Fig. 3b, and their separation distance is ~0.19 nm, which is similar to the separation distance of Mg-rich columns in the η_1 phase shown in Fig. 3c. Based on these analyses, it is proposed that these three atomic columns marked by white circles in Fig. 3a are rich in Mg atoms. In addition, the intensity profile of the line drawn from a Mg-column at the η_1/Al matrix interface to an adjacent Al-column in the aluminium matrix is shown in Fig. 3d. It shows that the intensity of the Mg-column is approximately half of the intensity of the nearby Al-column. This is because the Mg atom concentration in the Mg-column is less dense (approximately half in number density) than Al atom concentration in the Al-column. A 3D model of this interface structure built based on the experimental observations is shown in Fig. 3e. Fig. 3f–g are simulated HAADF-STEM images of the η_1/Al interface viewed along $[1\bar{2}10]_{\eta_1}$ and $[0001]_{\eta_1}$, which fit well with experimental observations.

To further understand the segregation of solutes in the η_1/Al interface, a further examination was made of the energetic stability of Mg and Zn atoms segregated at the η_1/Al interface. The formation energy, E_f, of this interface was calculated using the following equation:

$$E_f = E_T - N_\eta E_\eta - \sum_i N_i E_i$$

where E_T is the calculated total energy of the supercell, N_η is the number of unit cells of η_1 phase in the supercell, E_η is the formation energy of a unit cell η_1 phase, E_i (i = Al, Zn or Mg) is the formation energy of an Al, Mg or Zn atom in its ground state structures, and N_i is the number of atoms of each element included in the supercell, excluding atoms in the η_1 phase. Three models were built for comparison, as shown in Fig. 4a. Model I was proposed by

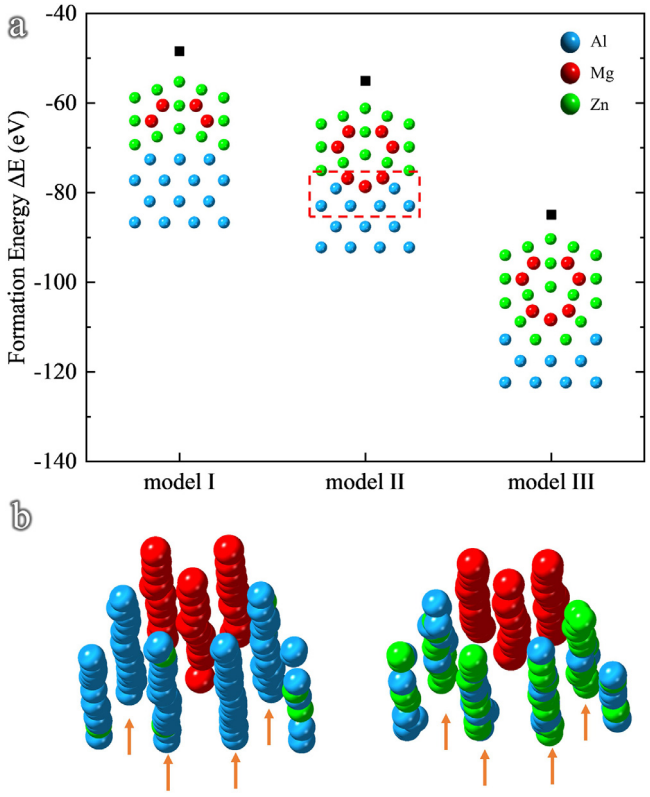

Fig. 4. (a) Calculated formation energies of three structures of the η_1/Al habit plane interface. (b) Hybrid Monte Carlo and molecular dynamics (MC and MD) simulation showing segregation of Zn atoms to the η_1/Al interface. Left diagram represents model II (marked by the frame in (a)), which is the initial stage of the simulation; Right diagram represents model III, which is the thermodynamic equilibrium state reached in the hybrid MC and MD simulation.

Bendo et al. [6]. Based on our experimental results, we proposed model II and model III. There is no Zn or Mg segregation in the η_1/Al interface in model I, which has the highest formation energy of the interface. In model II, the Al atoms outside the concave of the zig-zag Zn-rich layer in model I are changed to three columns of Mg, and the interface formation energy is lower than that of model I. In model III, Zn atoms have substituted Al atoms near the Mg atoms it the interface in model II, and the resultant interface is the most energetically favored among the three models. Therefore, the site-specific solute segregation observed in the present work is energetically driven. The Zn segregation in the η_1/Al interface was further supported by a hybrid MC and MD simulation. The initial structure of the η_1/Al interface for the hybrid MC and MD simulation is shown on the left part of Fig. 4b, where Zn atoms randomly substitute Al atoms in the Al matrix and form Al-Zn random solid solution. After the thermodynamic equilibrium state is reached, most of Zn atoms diffuse to the four atomic columns, indicated by orange arrows in Fig. 4b. This simulation suggests that the segregation of Zn atoms to these four atomic columns is energetically favourable.

In summary, co-segregation of Mg and Zn atoms occurs in the η_1/Al interface that is parallel to the $\{002\}_\alpha$ habit plane of η_1 precipitate. The outmost layer of η_1 phase is a zig-zag Zn-rich layer, followed by two atomic layers comprising segregated Mg and Zn atoms. The segregated Mg atoms locate at the inner layer adjacent to the concave of the zig-zag layer, while the segregated Zn atoms locate at both layers adjacent to the segregated Mg atoms. Energy calculations with the accuracy of density functional theory, and simulations made by hybrid MC and MD, suggest that these segregations are energetically favoured.

Declaration of Competing Interest

The authors declare that they have no known competing financial interests or personal relationships that could have appeared to influence the work reported in this paper.

Acknowledgments

The authors are grateful to the financial support from the Australian Research Council. B. Cheng wishes to thank Monash University for Monash Graduate Scholarship and Faculty of Engineering International Postgraduate Research Scholarship. This work is also financially supported by National Natural Science Foundation of China (51771036, 51131009 and 51421001), National Key Research and Development Program of China (2016YFB0700402). This work is supported by computational resources from Pawsey allocated through the National Computational Merit Allocation Scheme.

References

[1] Y. Komura, K. Tokunaga, Acta Crystallogr. B 36 (7) (1980) 1548–1554.
[2] J. Gjønnes, C.J. Simensen, Acta Metall. Mater. 18 (8) (1970) 881–890.
[3] T.F. Chung, Y.L. Yang, M. Shiojiri, C.N. Hsiao, W.C. Li, C.S. Tsao, Z. Shi, J. Lin, J.R. Yang, Acta Mater. 174 (2019) 351–368.
[4] T.F. Chung, Y.L. Yang, B.M. Huang, Z. Shi, J. Lin, T. Ohmura, J.R. Yang, Acta Mater. 149 (2018) 377–387.
[5] X. Xu, J. Zheng, Z. Li, R. Luo, B. Chen, Mater. Sci. Eng. A 691 (2017) 60–70.
[6] A. Bendo, K. Matsuda, S. Lee, K. Nishimura, N. Nunomura, H. Toda, M. Yamaguchi, T. Tsuru, K. Hirayama, K. Shimizu, J. Mater. Sci. 53 (6) (2018) 4598–4611.
[7] L.J. Allen, A.J. D'Alfonso, S.D. Findlay, Ultramicroscopy 151 (2015) 11–22.
[8] L. Zhang, J. Han, H. Wang, R. Car, E. Weinan, Phys. Rev. Lett. 120 (14) (2018) 143001.
[9] L. Zhang, D.Y. Lin, H. Wang, R. Car, Phys. Rev. Lett. 3 (2) (2019) 023804.
[10] G. Kresse, J. Furthmüller, Phys. Rev. B 54 (16) (1996) 11169–11186.
[11] P.E. Blöchl, Phys. Rev. B 50 (24) (1994) 17953–17979.
[12] G. Kresse, D. Joubert, Phys. Rev. B 59 (3) (1999) 1758–1775.
[13] J.P. Perdew, K. Burke, M. Ernzerhof, Phys. Rev. Lett. 77 (18) (1996) 3865–3868.
[14] J.S. Smith, B.T. Nebgen, R. Zubatyuk, N. Lubbers, C. Devereux, K. Barros, S. Tretiak, O. Isayev, A.E. Roitberg, Nat. Commun. 10 (1) (2019) 2903.
[15] G.P.P. Pun, R. Batra, R. Ramprasad, Y. Mishin, Nat. Commun. 10 (1) (2019) 2339.
[16] S. Plimpton, J. Comput. Phys. 117 (1) (1995) 1–19.
[17] S.J. Kang, Y.W. Kim, M. Kim, J.M. Zuo, Acta Mater. 81 (2014) 501–511.
[18] L. Reich, M. Murayama, K. Hono, Acta Mater. 46 (17) (1998) 6053–6062.
[19] K. Matsuda, D. Teguri, Y. Uetani, T. Sato, S. Ikeno, Scr. Mater. 47 (12) (2002) 833–837.
[20] L. Bourgeois, C. Dwyer, M. Weyland, J.F. Nie, B.C. Muddle, Acta Mater. 59 (18) (2011) 7043–7050.
[21] J.M. Rosalie, L. Bourgeois, Acta Mater. 60 (17) (2012) 6033–6041.
[22] M. Fiawoo, X. Gao, L. Bourgeois, N. Parson, X.Q. Zhang, M. Couper, J.F. Nie, Scr. Mater. 88 (2014) 53–56.
[23] V. Araullo-Peters, B. Gault, F.d. Geuser, A. Deschamps, J.M. Cairney, Acta Mater. 66 (2014) 199–208.
[24] C. Liu, H. Chen, J.F. Nie, Scr. Mater. 123 (2016) 5–8.
[25] D. Rossouw, B. Langelier, A. Scullion, M. Danaie, G.A. Botton, Scr. Mater. 124 (2016) 174–178.
[26] J. Miao, W. Sun, A.D. Klarner, A.A. Luo, Scr. Mater. 154 (2018) 192–196.
[27] C.Q. Liu, H.W. Chen, N.C. Wilson, J.F. Nie, Scr. Mater. 163 (2019) 91–95.